MATERIALS CHEMISTRY FRONTIERS

RESEARCH ARTICLE

View Article Online
View Journal

Cite this: DOI: 10.1039/d5qm00932d

Integrated theoretical and experimental study of boron antimonide: structural, optical, and thermoelectric properties

J. Kiruthika,[a] S. Nanthini,[ab] Parkavi V,[ac] M. Manjula,[d] H. Shankar,[b] Lakshmi Prabha Chandrasekar,[ae] Arathyram Ramachandra Kurup Sasikala,[f] Suhasini Sathiyamoorthy,*[g] Afeesh Rajan Unnithan*[f] and Pandiyarasan Veluswamy*[ae]

Boron antimonide (BSb), a promising thermoelectric material from the binary Group III–V compounds, was synthesized using a hydrothermal method. It represents the first report on the chemical synthesis of BSb. This study combines experimental and theoretical methods, utilizing the full potential linearized augmented plane wave (FP-LAPW) and the Perdew–Burke–Ernzerhof generalized gradient approximation (PBE-GGA) to calculate its structural, electronic, optical, and thermoelectric properties. The investigation explores the influence of different molar ratios of elemental boron and antimonide nanoparticles on the material structure and electrical and thermal properties. X-ray diffraction (XRD) revealed the zinc blende structure of BSb. UV-visible studies was used to determine the bandgap energy found the highest of 2.91 eV for the 1 : 2 ratio among other molar ratios. Hall measurements revealed an electrical conductivity of 6.52 × 10^{-3} Sm^{-1} for the 1 : 2 ratio, while Seebeck measurements yielded a maximum Seebeck coefficient of −778 μV K^{-1} for the 1 : 2 ratio indicating n-type behavior, which was consistent with both experimental Hall and Seebeck analysis. Using the BoltzTraP code, the Seebeck coefficient and power factor were determined to be 912 μV K^{-1} and 0.387 nW m^{-1} K^{-2}, respectively. The lowest experimental thermal conductivity of BSb was found to be 0.059 W m^{-1} K^{-1} for the 1 : 2 ratio due to the enhanced phonon scattering at the interfaces. These findings unveil intriguing thermal and electrical behaviors in the III–V boron group, showing promise for potential thermoelectric applications.

Received 28th December 2025,
Accepted 6th April 2026

DOI: 10.1039/d5qm00932d

rsc.li/frontiers-materials

1. Introduction

Utilizing waste heat for electricity has become crucial, as traditional energy sources approach their limits. Thermoelectric (TE) materials have emerged as an interesting area of research due to their ability to convert waste heat into electricity without the need for moving parts. Boron-based compounds have emerged as promising candidates among the materials being studied due to their high thermal conductivity, stability, and refractory nature, making them ideal for high-temperature applications. The complex chemistry of elemental boron contributes to the structural intricacy of these materials, which have been discovered and continuously studied using diverse synthesis techniques over recent decades.[1] Boron compounds particularly those belonging to the Group III–V compound family, serve as the foundation for a wide range of well-established and emerging technologies due to their distinct electronic,[2] elastic,[3] and structural properties over conventional materials. Among them, boron pnictides like boron phosphide (BP),[4] boron arsenide (BAs),[5] and boron antimonide (BSb)[6]

[a] SMart and Innovative Laboratory for Energy Devices, Indian Institute of Information Technology Design and Manufacturing, Kancheepuram, Chennai, 600127, Tamilnadu, India. E-mail: pandiyarasan@yahoo.co.in
[b] Department of Physics, KPR Institute of Engineering and Technology, Coimbatore, 641407, Tamilnadu, India
[c] School of Interdisciplinary Design and Innovation, Indian Institute of Information Technology Design and Manufacturing Kancheepuram, Chennai, 600127, Tamilnadu, India
[d] Department of Physics, Sathyabama Institute of Science and Technology, Chennai, 600119, Tamilnadu, India
[e] Department of Electronics and Communication Engineering, Indian Institute of Information Technology Design and Manufacturing Kancheepuram, Chennai, 600127, Tamilnadu, India
[f] Centre for Pharmaceutical Engineering Science, School of Pharmacy, Optometry and Medical Sciences, Faculty of Health and Social Care, University of Bradford, BD7 1DP, UK. E-mail: a.rajanunnithan@bradford.ac.uk
[g] School of Electronics Engineering, Vellore Institute of Technology, Chennai, 600127, Tamilnadu, India. E-mail: suha.sathiya@gmail.com

stand out due to their unusual physical and chemical properties. This unique behavior arises from the boron atom's small size and deficiency of core p electrons. These properties include shorter bonds, exceptional strength, and a wide range of band gaps, and because of these characteristics, boron compounds find applications in a wide range of electronic and optoelectronic devices such as lasers[7] and detectors.[8]

The most extensively studied compounds in this category are boron nitride (BN)[9] and BP.[10] While BAs have been investigated experimentally to a limited extent, BSb and boron bismuth (BBi)[11] are yet to be chemically synthesized, with the majority of research on these compounds relying on theoretical methods. During the past decade, researchers have continuously explored a few different synthesis techniques to discover and investigate these materials. The continued effort to develop innovative synthesis methods is driven by the prospect of these materials achieving enhanced figure of merit (zT) that surpass those previously documented in the literature. Optimizing these under-explored materials presents a significant opportunity to address the growing need for efficient energy harvesting solutions, for the solid state particularly in TE technology, in which conversion of temperature differences into electricity, relies on the material zT value, determined by factors like the Seebeck coefficient (S), electrical resistivity (ρ), total thermal conductivity (κ), and absolute temperature (T). Thermoelectric devices work on the principle of the Seebeck effect. This principle states that a voltage difference is generated across two dissimilar materials when subjected to a temperature gradient.[12,13]

In this regard, few theoretical calculations of BSb have been conducted in the last decade. Theoretical investigation of the structural and electronic properties of BSb in the zinc blende (ZB) structure was carried out by M. Ferhat *et al.* However, the approach was unable to describe the energy of the excited states accurately.[14] A. Zaoui *et al.* discussed the structural and electronic properties of BSb, using the full potential linearized augmented plane wave method (FP-LAW) in which BSb was confirmed to have a ZB structure. In this method, the generalized gradient approximation was used for the exchange–correlation potential.[15] The highly covalent nature and low phonon scattering of diamond persuaded researchers to theoretically study the physical properties of BX (X = N, P, As, Sb, and Bi) compounds using density functional theory (DFT) calculations by replacing one carbon with a III-group element and another with a V-group element.[16] Yao *et al.* utilized the *ab initio* method to study bulk boron antimonide (BSb), which has significant potential as a hot carrier absorber (HCA) due to its phononic structure, which is distinguished by the inhibition of phonon decay.[17] Somaieh Ahmadi *et al.* presented the lowest Seebeck coefficient (S = 1.8 × 10^{18} μV K^{-1}) and intrinsically highest power factor (PF = 0.95 W m^{-1} K^{-2}) of BSb among graphene counterparts BX (X = P, As and Sb) using first-principles calculations using the Boltzmann method.[18] Recently, Vladimir L. Solozhenko *et al.* explored the geometry and ground state energy of hexagonal boron pnictides BX (X = As, Sb, Bi) and reported a quartz-derived phase of BSb as dynamically stable at ground state based on quantum DFT.[19]

Despite numerous theoretical studies on the structural, electronic, and optical properties of BSb using first-principles methods, experimental investigations of these materials remain limited. Fig. 1 provides an overview of previous research techniques on BSb using a top-down approach. S. N. Das *et al.* were the first to report on the synthesis of ZB–BSb in thin film form using rapid thermal annealing (RTA). They deposited elemental boron and antimony onto a fused silica substrate *via* e-gun deposition.[20] The complete BSb film synthesis was achieved through annealing at 773 K and confirmed by a characteristic X-ray diffraction (XRD) peak. After RTA, the multiple layers with a thickness of 22 nm were transformed into B/Sb or Sb/B films, each with a 1 : 1 stoichiometric ratio of B : Sb, as quantified by X-ray photoelectron spectroscopy (XPS). S. Dalui *et al.* prepared BSb films on fused silica substrates using the co-evaporation method, successfully replicating BSb films consistent with prior work by S. N. Das. Their research included a detailed analysis of temperature dependent conductivity, as well as a comprehensive characterization of the films through spectroscopic and optical methods.

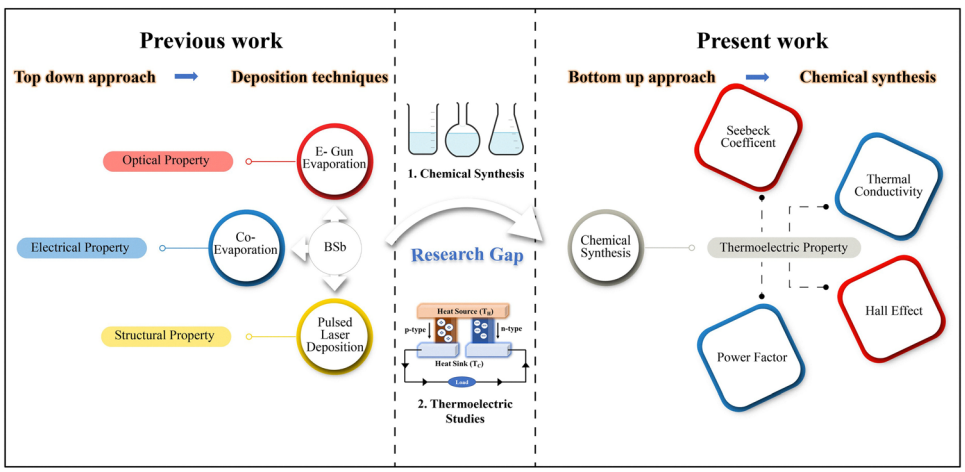

Fig. 1 Schematic summarizing past BSb synthesis efforts and highlighting the advancements of the present study.

The absorption coefficients of the BSb films were calculated based on transmittance and reflectance measurements, and the data revealed an indirect electronic transition with a bandgap closely matching values predicted by *ab initio* calculations. Additionally, the extinction coefficient measured from transmittance showed that the films are highly absorbent. Furthermore, electrical conductivity measurements using the four-probe technique showed that the films were highly resistive.[21] Subsequently, research was conducted by S. Das *et al.* which remains the most recent experimental approach using pulsed lasers for the deposition of BSb films for hot carrier solar cell device applications. Films were deposited on three different substrates at different temperatures (473 K, 573 K, and 673 K) using a Nd-YAG laser. Grain sizes increased for films when deposited at higher substrate temperatures during deposition. XRD patterns indicated a polycrystalline nature with a ZB–BSb structure, consistent with previous studies. Optical studies revealed an indirect bandgap. A modified KK theory approach, as described by Xue *et al.*,[22] was employed to determine film thickness, refractive index, and extinction coefficient. This analysis indicated that lower deposition temperatures resulted in denser films.[23]

In this study, a comprehensive investigation was conducted, using both theoretical and experimental methodologies, to explore the thermoelectric potential of BSb materials for the first time using a bottom-up approach also known as chemical synthesis. Despite its promising potential as a Group III–V semiconductor, with advantages in the acoustic phonon branch, BSb synthesis and characterization remain challenging due to the significant mass difference between boron and antimony atoms. Consequently, there are limited reports on its synthesis and characterization. The hydrothermal synthesis was employed as a bottom-up chemical approach, offering several advantages over the physical deposition techniques previously reported for BSb. Earlier methods such as rapid thermal annealing, co-evaporation, and pulsed laser deposition successfully confirmed the zinc blende structure of BSb but faced recurring challenges, including deviations from stoichiometry due to the large differences in vapor pressures and atomic masses of boron and antimony. These techniques also required high processing temperatures (473–773 K) followed by annealing, which increases energy consumption and risks introducing thermal stress. In contrast, the hydrothermal method allows boron and antimony precursors to mix homogeneously in solution before crystallization, enabling precise stoichiometric control and crystal growth at relatively low temperatures ($\sim$423 K) under autogenous pressure. Importantly, this approach produces gram scale quantities of BSb powders that can be sintered into pellets, facilitating bulk thermoelectric measurements that are difficult to achieve with thin films. Additionally, the method provides tunable control over particle size and morphology through adjustments of reaction parameters, while remaining cost-effective and environmentally benign, making it a desirable route for the first chemical synthesis of BSb. To address the challenges associated with synthesizing BSb such as defects, precise stoichiometric balance and optimizing it as a thermoelectric material, this research endeavours to investigate the behavior of chemically synthesized BSb and its thermoelectric properties.

In this study, we first used DFT simulations to investigate the structural, electronic, and thermoelectric properties of BSb, using the BoltzTraP code for detailed analysis. Then we synthesized BSb experimentally and validated the computational predictions through comprehensive structural, electronic, and thermoelectric measurements.

2. Materials and methods

The computational work involved self-consistent *ab initio* calculations using the FP-LAPW method in the Wien2k code, with the Perdew–Burke–Ernzerhof (PBE) and generalized gradient approximation (GGA) for structural optimization, to explore the structural, electronic, and thermoelectric properties of BSb. The experimental work was conducted using the hydrothermal method, followed by annealing in an argon atmosphere. Subsequent characterization studies were carried out to analyze the nature and properties of the material.

Sodium borohydride ($NaBH_4$) and antimony trichloride ($SbCl_3$) were purchased from Sigma Aldrich, India with high purity. Concentrated hydrochloric acid (Con.HCl $\geq$ 35.40%) was obtained from Rankem, India. Deionized water was used as the solvent. To synthesize BSb, 20 mL of 0.5 M $NaBH_4$ solution prepared in deionized water was stirred at 300–400 rpm. 20 mL of 0.5 M $SbCl_3$ solution prepared in deionized water and 10 mL concentrated HCl was kept under stirring for 10–15 minutes separately. The $NaBH_4$ solution was added dropwise to the $SbCl_3$ solution in an ice bath to control the exothermic reaction, forming a black precipitate. After 1 hour, the mixture was transferred to a Teflon-lined autoclave and heated at 423 K for 12 hours. The cooled sample was washed, dried at 343 K for 6 hours, and sintered at 773 K in an argon atmosphere for 3 hours. Details of the synthesis method and physical mechanism are discussed in the SI. The dried powders, synthesized in 1 : 1, 1 : 2, and 2 : 1 molar ratios of boron and antimony (S1, S2, S3), were pressed into pellets for further characterization. The chemical synthesis process for BSb is illustrated in Fig. 2.

3. Computational design and experimental study of BSb

The FP-LAPW method, as implemented in the Wien2k code, was used to investigate the structural, electronic, and thermoelectric properties of BSb. PBE and GGA was used for optimization of the BSb structure. The muffin–tin radius values are set to be R_{MT} (B) = 1.69 a.u. and R_{MT} (Sb) = 2.35 a.u. The valence wave functions inside the muffin–tin spheres are expanded up to l_{max} = 10 and the Fourier coefficient of charge density is selected as G_{max} = 12 (a.u.)$^{-1}$. The modified Becke–Johnson functionals (mBJ–GGA) exchange–correlation potential is used to calculate the exchange and correlation energy of electrons. The 10 $\times$ 10 $\times$ 10 Monkhorst–pack mesh is used for the

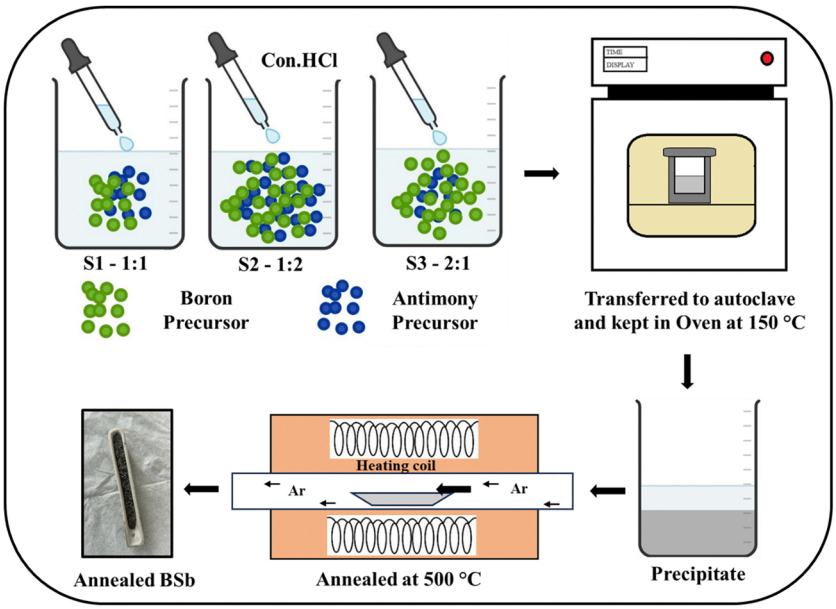

Fig. 2 Schematic representation for the chemical synthesis of BSb.

Brillouin-zone integration. In order to attain energy eigenvalue convergence, the expansion of wavefunctions in the interstitial region were made with a cut-off K_{max} = 7/R_{MT}. An energy convergence criterion of 0.0001 Ry was employed to distinguish between core and valence states and a charge convergence criterion of 0.001 eV was maintained. To analyze the behavior of charge carriers, a Hall experiment was conducted using the BoltzTraP code, and the electrical conductivity (σ/τ), electrical resistivity (ρ), mobility (μ) and carrier concentration (n) are studied for the considered compound. A theoretical approach was employed using BoltzTraP, which solves the semi-classical Boltzmann transport equation within the relaxation-time approximation. This theoretical method allows for the calculation of transport coefficients, such as electrical conductivity, Seebeck coefficient and power factor, by integrating over the electronic states derived from DFT.

3.1 Structural and morphological study

Fig. 3(a) displays the cubic structure of BSb, where blue and green spheres represent boron and antimony atoms, respectively. The binary BSb material crystallizes in the cubic space group 216 ($F43m$) with the experimental lattice constant of a_{exp} = 5.234 Å and the calculated lattice constant of a_{cal} = 5.286 Å. The boron atom occupies the position X = 0, Y = 0, Z = 0 and the antimony atom occupies the position of X = 0.25, Y = 0.25, Z = 0.25. The volume optimization curve for BSb is presented in Fig. 3(b). From the optimized total energy obtained from this curve, the fitted lattice constant can be derived. To determine the most stable volume of the cubic structure, the total energy of the BSb unit cell was computed by varying the cell volume by −10%, −5%, 0%, +5%, and +10% around the experimental volume, yielding an optimal volume of 249.29.[24] The volume optimization curve in Fig. 3(b) was obtained by fitting the total energy and corresponding unit cell volumes to the Birch–Murnaghan equation of state. Table 1 summarizes the lattice constant, space group, crystal structure, total energy (E_0) and Fermi energy (E_F) of BSb. The core and valence electrons of boron and antimony are $1s^2$ and ($1s^2 2s^2 2p^6 3s^2 3p^6\ 3d^{10} 4s^2 4p^6$) and ($2s^2 2p^1$) and ($4d^{10} 5s^2 5p^3$) respectively. The total energy of the system was calculated to be −13 016.929 Ry, with a Fermi energy of 0.527 Ry. Bandgap values calculated using three different exchange–correlation potentials GGA(Γ − X), GGA (Γ − L), mBJ, and GGA+U (U = 0.52 eV) are 0.763 eV, 2 eV, 1.133 eV, and 0.865 eV, respectively.[25]

The computational design on the structure of BSb was verified by performing XRD and the patterns of BSb at various molar ratios are shown in Fig. 3(c). XRD is used to study the phase composition and crystal structure. All primary diffraction peaks exhibit strong consistency across different molar ratio. Among the two potential stoichiometric compositions (rock salt and ZB) of BSb, the ZB-cubic crystal system is confirmed with a space group of $F43m$, with computational calculations as mentioned in Table 1. XRD analysis identifies prominent peaks at 2θ = 19.7°, 25.9°, and 27.9°, corresponding to diffraction planes (113), (122) and, (107) respectively, which are indicative of boron. This is confirmed by the JCPDS card number 89-277.[27] Furthermore, the diffraction peaks of Sb, indicated by indices such as (012), (104), (110), and others, correspond to specific 2θ values of 28.8°, 40.2° and 42° respectively, which are consistent with JCPDS entry 35-0732.[28]

These findings align with established data, confirming the presence of elemental boron and antimony in the prepared sample. The low-intensity peak observed near 2θ = 13.93° corresponds to chlorine oxide, specifically Cl_2O_7, as identified by JCPDS entry 78-2455. This likely arises from incomplete reduction, resulting in a small amount of residual oxide. The low intensity and limited distribution of Cl_2O_7, and its impact on the structural and electronic properties of the sample is

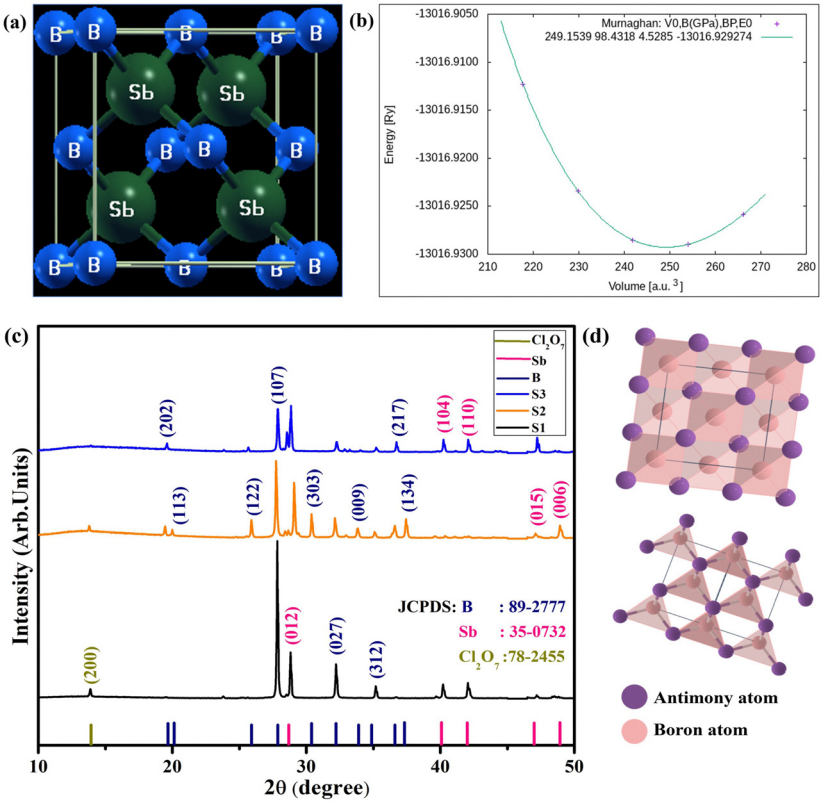

Fig. 3 (a) Crystal structure of BSb and (b) volume optimization curve depicting the equilibrium volume of BSb. (c) The X-ray diffraction pattern of BSb and (d) the cubic structure of BSb. The violet circle represents the antimony atom and pink circle represents the boron atom.

Table 1 Structural properties of BSb

Compound	BSb
Lattice constant (Å)	a_{exp} = 5.234 a_{cal} = 5.286 5.2809,[24] 5.279[26]
Space group	216 – $F43m$
Structure	Cubic
Volume (Bohr^3)	249.29
Bulk modulus (GPa)	97.54
E_0 (Ry)	−13 016.929
E_g (eV)	0.763 (GGA) (Γ − X) 2 (GGA) (Γ − L) 1.133 (mBJ) 0.865 (GGA + U)
E_F (Ry)	0.527

expected to be negligible. Chlorine oxides like Cl_2O_7 are generally volatile and unstable, and any minor presence is unlikely to interfere with the primary boron and antimony phases, which show prominent, well-defined diffraction peaks in the XRD analysis. Despite changes in the molar ratio, the samples S1, S2 and S3 maintain the same crystal structure in the crystal lattice without any phase shifts. Furthermore, the morphology of BSb was examined and a detailed discussion is provided in the SI.

3.2 Exploring the band behaviour

For electronic band structure calculation, experimental lattice parameters are used with the exchange–correlation potential. Fig. 4(a–c) depict the total density of states (DOS) and the partial DOS of BSb. From Fig. 4, the DOS below the Fermi level is due to B-s, p states and Sb-s, p states, and above the Fermi level is contributed mainly by B-p states and Sb-p, d states, and there is a small contribution of Sb-D-t_{2g} and f-states. The band structure of BSb, shown in Fig. 4(d), reveals an indirect band-gap configuration, with the valence band maximum (VBM) and conduction band minimum (CBM) located at different K points in the Brillouin zone. Specifically, the VBM is positioned at the 'Γ' point, while the CBM is located near the 'X' point along the Δ-line, resulting in an indirect bandgap of 1.13 eV at $\Gamma - \Delta_{min}$.

The lowest sharp band in the conduction band is due to the electron effective mass, whereas along the same symmetry, the maximum of the valence band is a hybrid of flat and sharp bands. The combination of flat and sharp bands enhances the electron transport, as the sharp band is responsible for the higher value of electron electrical conductivity. Fig. 4(e and f) and (g and h) represent the flat band of boron s,p-states, antimony s,p-states respectively. Fig. 4(f and h) reveal that the VBM in BSb arises from the hybridization of boron p-states with antimony p-states, while the CBM is primarily due to strong hybridization between boron s-states and antimony p-states. This hybridization exhibits a sp^3 characteristic, indicating the covalent bonding nature of BSb. In this hybridisation, there is only a little contribution of boron p-states and antimony s-states. The calculated band gap values with mBJ–GGA are in agreement with previous first principles calculations.[26]

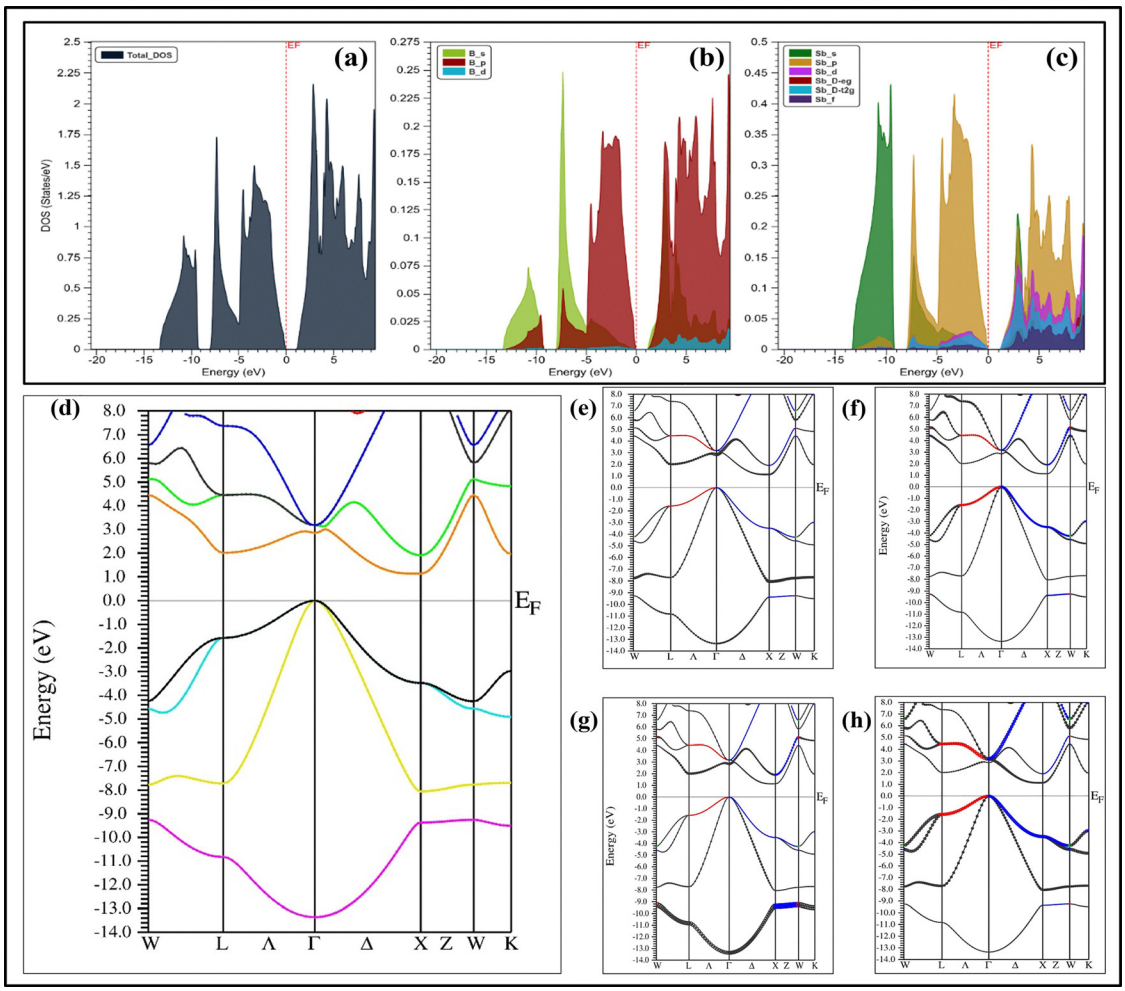

Fig. 4 (a) Total density of states of BSb, with partial density of states for (b) B and (c) Sb and (d) the band structure of BSb and fat band structure of (e) B-s, (f) B-p, (g) Sb-s and (h) Sb-p states.

3.3 Optical properties

The optical properties are characterized by the complex dielectric function, $\varepsilon(\omega)$, which describes the linear response of the system to an external electromagnetic field with a small wavevector. Once this function is calculated, other optical properties can be accurately determined. $\varepsilon(\omega)$ can be expressed as:

$$\varepsilon(\omega) = \varepsilon_1(\omega) + i\varepsilon_2(\omega) \quad (1)$$

Here ε_1 and ε_2 are real and imaginary parts of the dielectric function respectively. The following optical properties namely dielectric constant (real and imaginary), absorption coefficient, Sigma (conductivity), energy loss, extinction coefficient, refractive index and reflectivity are calculated for BSb as shown in Fig. 5(e–h). The dielectric function which includes real and imaginary parts is determined by transition between the valence and conduction band. In this, the real part $\varepsilon_1(\omega)$ represents the optical dispersion and the imaginary part $\varepsilon_2(\omega)$ represents absorption of the crystal. The static dielectric constant, $\varepsilon_0(\omega)$, which strongly depends on the energy gap, is approximately 9.5 eV for BSb (Fig. 5a). Within the photon energy range of 2–13.5 eV, the dominant peak appears at 4.8 eV for BSb. In Fig. 5(b), $\varepsilon_2(\omega)$ approaches nearly zero around 13.5 eV, indicating minimal photon absorption at this energy. Fig. 5(c) shows that the absorption spectrum of BSb begins near 2.5 eV. The optical conductivity of BSb reaches a maximum of approximately 17 000 S m^{-1} at 5 eV (Fig. 5d), suggesting its potential use in solar cell applications, as this peak occurs within the visible range.

The energy loss function, which describes the energy lost by fast-moving electrons, has a main peak around 12 eV (Fig. 5e). From the extinction coefficient graph (Fig. 5f), the local maxima of $K(\omega)$ corresponding to the zero of $\varepsilon_1(\omega)$ is found at 3.4 at 5.0 eV. The zero-frequency refractive index $n(0)$ is found to be 3.1 for BSb as shown in Fig. 5(g). Reflectivity which varies with energy, exhibits multiple peaks. In Fig. 5(h), the maximum reflectivity, R_{max} = 0.65 occurs at 8.1 eV, and the minimum reflectivity, R_{min} = 0.55 appears at 9.2 eV. The optical properties of BSb, including high absorption in the visible-UV range, significant dielectric response, and peak optical conductivity, suggest that it could be employed for thermoelectric applications. The observed peaks in the dielectric and

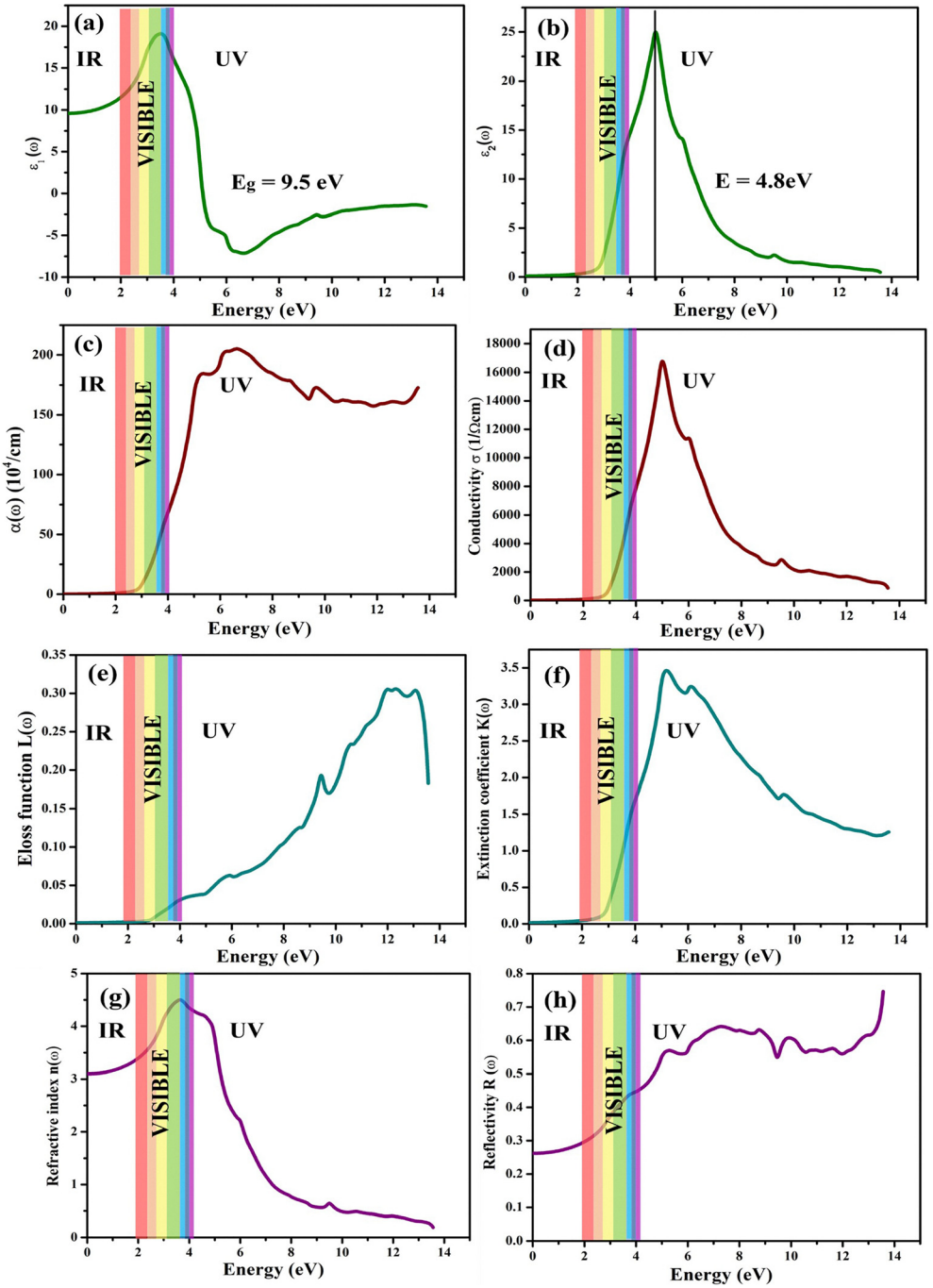

Fig. 5 Optical properties of BSb as a function of photon energy: (a) real part of the dielectric function ε_1, (b) imaginary part ε_2, (c) absorption coefficient $\alpha(\omega)$, (d) conductivity $\sigma(\omega)$, (e) energy loss function $L(\omega)$, (f) extinction coefficient $K(\omega)$, (g) refractive index $n(\omega)$, and (h) reflectivity $R(\omega)$.

conductivity spectra indicate strong electron–photon interactions and efficient charge transport, both of which are advantageous for thermoelectric performance, as they support enhanced energy conversion and minimal thermal conductivity in the material.

In this study, the bandgap of BSb was estimated to be 2.08 eV for S1, as depicted in Fig. 6(a) within the Tauc plot. Similar graphical representations were generated for other molar ratios, with respective bandgap energies derived from the Tauc plot (inset from Fig. 6 (a–c)). Consequently, it can be inferred from the optical investigation that the bandgap of BSb synthesized chemically ranges from 2.08 to 2.91 eV for indirect transitions, with the highest bandgap achieved at S2.[29] The increase in E_g with the increasing molar ratio can be attributed to the appreciable electronegative difference of B and Sb. Strong absorption in the visible region with an absorption edge at 400 nm (E_g = 2.91 and 2.32 eV) is shown in Fig. 6(S2 and S3). This increase in bandgap further separates the valence and

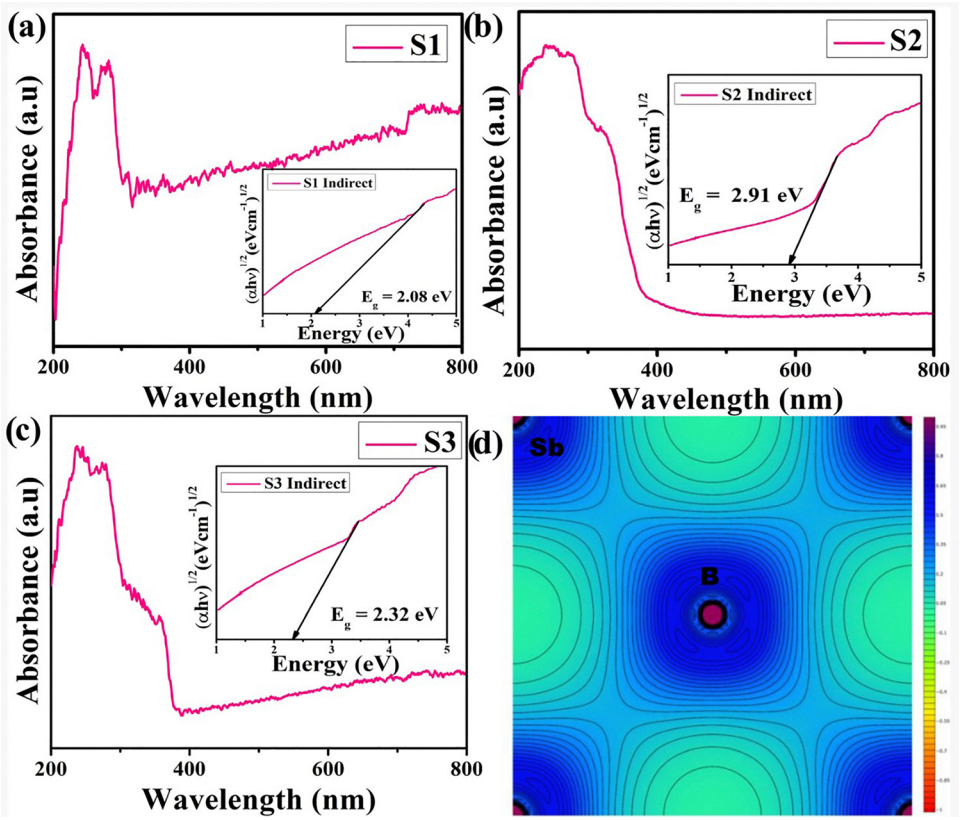

Fig. 6 Absorption spectra with the Tauc plot for samples: (a) S1, (b) S2, (c) S3, and (d) charge density plot of BSb.

conduction bands, requiring higher energy for electron excitation from the valence to the conduction band, which results in a lower intrinsic carrier concentration at a given temperature. Lower carrier density can enhance the Seebeck coefficient, since fewer thermally excited carriers lead to a higher voltage per temperature gradient. Furthermore, a larger bandgap often aligns with reduced lattice thermal conductivity, as it minimizes the overlap between phonon and electron energy states, thereby decreasing electron–phonon interactions. Consequently, the wider bandgap enables the material to perform effectively at higher voltages, temperatures, and frequencies, which is expected to positively influence its thermoelectric properties, such as an improved Seebeck coefficient and reduced thermal conductivity.[30]

Fig. 6(d) shows the charge density plot for the [100] plane of BSb, which helps to explain the bonding nature between B and Sb atoms. The symmetric charge density distribution around the B and Sb atoms suggests a combination of weak covalent and ionic interactions. This bonding enhances the ductility of the material. The observed increase in mobility from S1 to S3 is primarily due to microstructural improvements, larger grain sizes, fewer grain boundaries, stronger covalent bonding, and reduced defect density, resulting in a clear conduction pathway for electrons. The reduction in scattering mechanisms dominates over the moderate change in carrier concentration, producing the observed increase in mobility.

4. Thermoelectric properties

4.1 Thermoelectric measurements

To analyze the behavior of charge carriers in a sample, a Hall experiment is typically conducted, as the inverse Hall coefficient is directly related to the charge carrier density. Using the BoltzTraP code, the electrical conductivity (σ/τ), electrical resistivity (ρ), mobility (μ) and carrier concentration (n) are studied for the considered compound. The values of all the above mentioned are calculated for the temperature range from 100 K to 300 K at Fermi energy. Graphs plotted between σ/τ, ρ, μ and n *versus* temperature (T) are presented in Fig. 7(a–d). From Fig. 7(a), maximum conductivity is achieved at 300 K. The mobility and carrier concentration increased with temperature and reaches a maximum value at 300 K consistent with the findings of Zhou *et al.*, in a comparative study of the thermoelectric performance of graphene-like BX (X = P, As, Sb) monolayers.[31] Additionally, the electrical properties and Hall values were examined and validated through experimental Hall-effect measurements to better understand the relationship between charge carriers, mobility, and conductivity with the details provided in the SI.

Using the BoltzTraP code, the thermoelectric properties such as Seebeck coefficient (S), electrical conductivity (σ) and power factor are studied for the considered compound. The values of Seebeck coefficient (S) and power factor are calculated

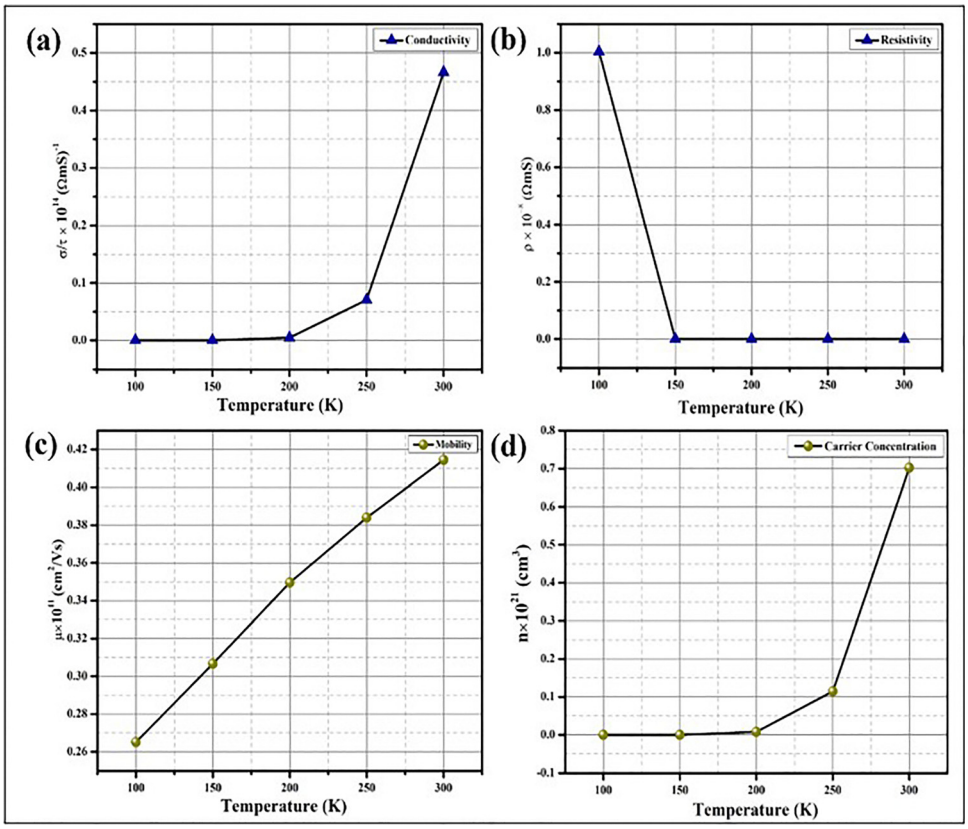

Fig. 7 (a) Electrical conductivity, (b) resistivity, (c) mobility, and (d) carrier concentration of BSb obtained from BoltzTraP calculations.

for the temperature range from 100 K to 300 K at the Fermi energy. Graphs are plotted between S *vs.* T and $S^2\sigma$ *vs.* T and presented in Fig. 8(a and b). The Seebeck coefficient known as the thermoelectric power, and the convention of the Seebeck coefficient depends on the majority charge carriers. In the present study, the considered BSb is found with holes as the majority charge carriers, and therefore the Seebeck coefficient become positive having 912 μV K^{-1} at 300 K, as shown in Fig. 8(a). This suggests that BSb is a p-type semiconductor. Here, there is a gradual decrease in Seebeck value from 100 K to 300 K. The electrical conductivity and power factor increases with respect to temperature. Considering the power factor, maximum value (0.387 nW m^{-1} K^{-2}) is obtained at 300 K as shown in Fig. 8(b). This is due to the excitation of minority carriers (*i.e.* electrons) at elevated temperatures. To investigate and validate the thermoelectric characteristics of BSb, Hall measurement and Seebeck measurement were conducted for the prepared sample. Resistivity and Hall measurements were conducted on BSb samples and detailed analysis is included in the SI. The Seebeck measurement involved creating a temperature gradient, a high temperature T_H and a low temperature T_L across the sample by maintaining a differential temperature of

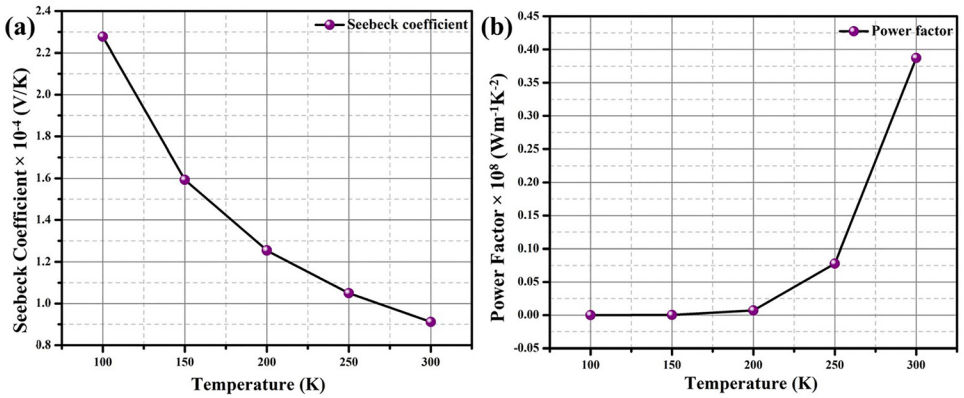

Fig. 8 (a) Seebeck coefficient and (b) power factor of BSb obtained from BoltzTraP calculations.

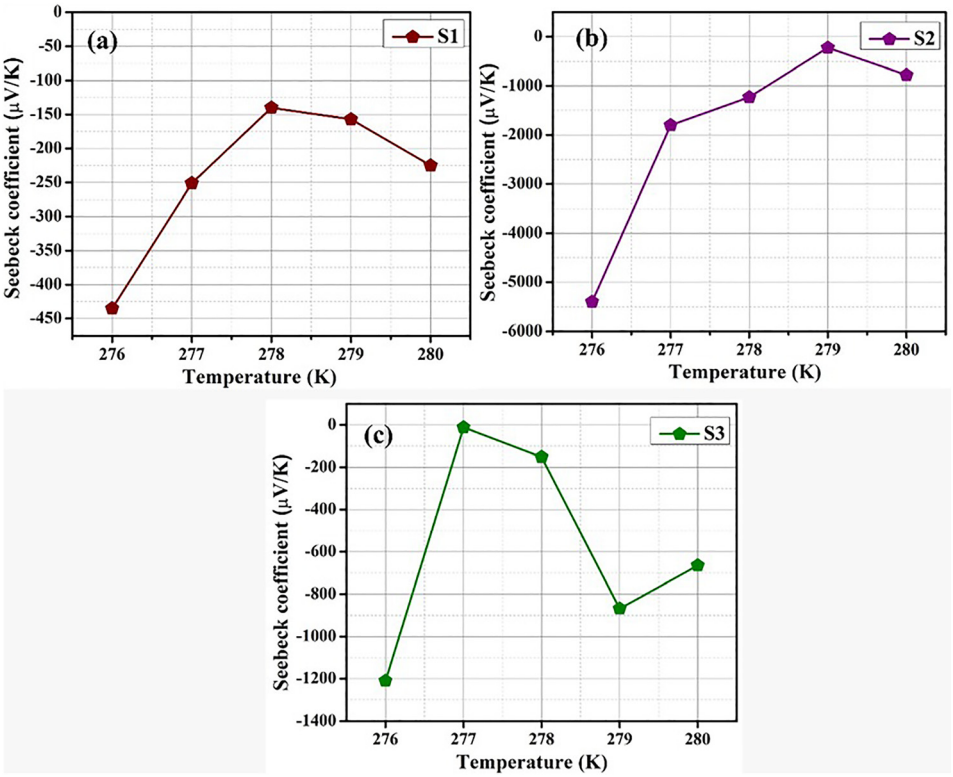

Fig. 9 The Seebeck coefficient *vs.* temperature difference for samples S1, S2, and S3 are shown in (a), (b) and (c), respectively, measured using a custom-built setup.

$\Delta T = T_H - T_L$ at its two ends. The Seebeck coefficient was recorded by varying the voltage values from 0 to 8 V. The temperature difference was maintained between 276.15 K and 280.15 K throughout the experiment. Fig. 9(a–c) effectively captures the trend across all three BSb molar ratios, the Seebeck coefficient exhibits a progressively stronger response with increasing input voltage. This indicates potential for these materials in applications where electrical input can be translated into a larger thermoelectric effect.

As discussed earlier, changes in molar concentration can influence interfaces and grain boundaries, both of which can influence decreasing the electrical conductivity and an enhanced Seebeck coefficient value.[32] The observed increase in the Seebeck coefficient is attributed to scattering at grain boundaries, as a result of the introduction of potential barriers.[33] The Seebeck coefficient (S) increases and then decreases with temperature in all BSb samples, consistent with diffusive carrier transport being the dominant mechanism over phonon drag within the studied range. The presence of interfaces and grain boundaries introduces weak potential barriers that preferentially scatter low energy carriers, producing an energy filtering effect that enhances the average carrier energy and increases S at moderately elevated temperatures. This effect is most pronounced in S2, which achieves an optimal balance between carrier concentration and interfacial scattering, yielding both the highest Seebeck response among the studied ratios. For example, at 280 K, S1 exhibits S = -225 μV K^{-1}, while S2 reaches -778 μV K^{-1}, confirming the positive effect of B : Sb ratio tuning.[34] The grain boundary scattering in S3 gives a sharp rise in Seebeck coefficient near 277 K, then drop, and partial recovery, showing that S3 exhibits strong temperature sensitivity compared to S2. Thus, according to Seebeck coefficient studies, the S2 ratio of the BSb material is ideal for achieving effective thermoelectric properties. The maximum Seebeck coefficient recorded was -778 μV K^{-1} at the S2 of BSb. The consistent negative Seebeck coefficient values across the readings suggest that the prepared BSb exhibits n-type semiconductor behavior, which aligns well with the Hall measurement. The thermoelectric performance evaluations are ongoing to further optimise the material's performance for potential device fabrication in the future.

5. Conclusion

The research presented here pioneers the successful chemical synthesis of BSb and also provides a comprehensive evaluation of its structural, electronic, and thermoelectric properties. Crystalline BSb nanoparticles were synthesized *via* a chemical method for the first time, with computational analysis identifying the binary BSb material as having a zinc blende structure within the 216 ($F43m$) cubic space group. UV-visible studies revealed a maximum bandgap energy of 2.91 eV for indirect transitions at a 1 : 2 ratio, consistent with density of states

(DOS) calculations. FTIR analysis along with the charge density diagram indicated the weak covalent and weak ionic nature of BSb. The band structure analysis of the Sb (p) orbitals indicates that these orbitals are the primary contributors to the electrical properties of the BSb material. This observation is further supported by the improved performance of BSb at a 1 : 2 ratio, suggesting that the Sb atoms play a crucial role in enhancing the material's electrical properties. The samples were identified as n-type semiconductors, and a Hall effect response was detected. Experimental Seebeck measurements revealed negative coefficients indicative of n-type semiconductor behavior, with a maximum value of -778 μV K^{-1} at a 1 : 2 ratio. Overall, the experimental findings suggest that the BSb material at the 1 : 2 ratio exhibits superior thermoelectric properties compared to other ratios investigated. The BoltzTraP code revealed the Seebeck coefficient and power factor to be 912 μV K^{-1} and 0.387 nW m^{-1} K^{-2}, respectively. These findings pave the way for further experimental exploration of BSb, with future research focusing on optimizing its thermoelectric properties through methods such as compositing, doping, or introducing defects.

Author contributions

Conceptualisation, formal analysis, methodology, validation, visualisation and writing original draft – Kiruthika J. and Nandhini S.; data curation – Dr Lakshmi Prabha Chandrasekar and Parkavi V.; investigation, software, writing review and editing, validation – Dr Manjula M.; conceptualisation, funding, resources, supervision, writing review and editing – Dr Pandiyarasan V.; formal analysis – Dr Shankar H.; formal analysis, investigation – Dr Suhashini S.; funding, resources, writing review and editing – Dr Arathyram R. K. S and Dr Afeesh R. U.

Conflicts of interest

The authors declare no competing interests.

Data availability

The data that support the findings of this study are available from the corresponding author upon reasonable request.

Supplementary information: synthesis, characterisation, SEM analysis, optical properties, FTIR spectroscopy, hall measurement, thermal conductivity and thermal effusivity. See DOI: **https://doi.org/10.1039/d5qm00932d**.

Acknowledgements

The authors would like to acknowledge the KPR Institute of Engineering and Technology, Coimbatore, India, for the grant of PhD fellowship. We would like to thank the Innovation in Science Pursuit for Inspired Research INSPIRE Faculty Program through the Department of Science and Technology (DST) funded by the Ministry of Science and Technology. (DST/INSPIRE/04/2017/002629), Indian Institute of Information Technology, Design, and Manufacturing, Kancheepuram for the financial support through SMIRE Project (IIITDM/SMIRE/2024/003) and SERB VRITHIKA for their valuable support. The authors would also like to acknowledge the Centre of Excellence for Advanced Materials Characterization, CFRD, KPR Institute of Engineering and Technology, Coimbatore, India, for their support of the research facilities.

References

1 K. Saglik, *et al.*, Thermoelectric Borides: Review and Future Perspectives, *Adv. Phys. Res.*, 2023, **2**, 2300010.
2 J. C. C. Fan, Thin films of iii-v compounds and their applications, *J. Phys., Colloq.*, 1982, **43**, 327–339.
3 S. Q. Wang and H. Q. Ye, First-principles study on elastic properties and phase stability of III - V compounds, *Phys. Status Solidi B*, 2003, **240**, 45–54.
4 J. Kang, *et al.*, Thermal Properties and Phonon Spectral Characterization of Synthetic Boron Phosphide for High Thermal Conductivity Applications, *Nano Lett.*, 2017, **17**, 7507–7514.
5 F. Tian and Z. Ren, High Thermal Conductivity in Boron Arsenide: From Prediction to Reality, *Angew. Chem.*, 2019, **131**, 5882–5889.
6 S. Cui, *et al.*, First-principles study on the boron antimony compound, *Phys. Status Solidi B*, 2009, **246**, 119–123.
7 K. Fauziah, *et al.*, Effect of phonon-boundary scattering on phonon-drag factor in Seebeck coefficient of Si wire, *AIP Adv.*, 2020, **10**, 7.
8 S. Almaviva, *et al.*, Improved performance in synthetic diamond neutron detectors: Application to boron neutron capture therapy, *Nucl. Instrum. Methods Phys. Res.*, 2010, **612**, 580–582.
9 N. Kumar and C. Bera, Enhanced thermoelectric performance of a wide-bandgap twisted heterostructure of graphene and boron nitride, *Nanoscale*, 2024, **16**, 7951–7957.
10 M. Li, *et al.*, Thermoelectric transports in pristine and functionalized boron phosphide monolayers, *Sci. Rep.*, 2021, **11**, 10030.
11 E. Deligoz, *et al.*, The first principles study on boron bismuth compound, *Comput. Mater. Sci.*, 2007, **39**, 533–540.
12 N. Abdul Rahim, *et al.*, Computational modeling and characterization of X-Bi (X = B, Al, Ga, In) compounds: Prospective optoelectronic materials for infrared/near infra applications, *Comput. Mater. Sci.*, 2016, **114**, 40–46.
13 S. Nanthini, *et al.*, Preparation and Characterization of Polyethylenimine Functionalized Reduced Graphene Oxide for Thermoelectric Applications, *ECS J. Solid State Sci. Technol.*, 2021, **10**(8), 081014, DOI: **10.1149/2162-8777/ac1e6c**.
14 M. Ferhat, *et al.*, First-Principles Study of Structural and Electronic Properties of BSb, *J. Phys.: Condens. Matter*, 1998, **10**, 7995.
15 A. Zaoui, *et al.*, Full Potential Linearized Augmented Plane Wave Calculations of Structural and Electronic Properties

of BN, BP, BAs and BSb, *J. Phys.: Condens. Matter*, 2001, **13**, 253–262.
16 M. Ustundag, *et al.*, The first-principles study on physical properties and phase stability of Boron-V (BN, BP, BAs, BSb and BBi) compounds, *Comput. Mater. Sci.*, 2014, **81**, 471–477.
17 Y. Yao, *et al.*, Investigation of boron antimonide as hot carrier absorber material, *Sol. Energy Mater. Sol. Cells*, 2013, **111**, 123–126.
18 S. Ahmadi, *et al.*, Thermoelectric Characteristics of Two-Dimensional Structures for Three Different Lattice Compounds of B-C-N and Graphene Counterpart BX (X = P, As, and Sb) Systems, *J. Phys. Chem. C*, 2021, **125**, 14525–14537.
19 V. Solozhenko, *et al.*, High-Pressure Phases of Boron Pnictides BX (X = As, Sb, Bi) with Quartz Topology from First Principles, *Crystals*, 2024, **14**, 221.
20 S. N. Das, *et al.*, Synthesis of B-Sb by Rapid Thermal Annealing of B/Sb Multilayer Films, *Bull. Mater. Sci.*, 2006, **29**, 549–552.
21 S. Dalui, *et al.*, BSb films: Synthesis and characterization, *J. Cryst. Growth*, 2007, **305**, 149–155.
22 S. Xue, *et al.*, Effects of Al doping concentration on optical parameters of ZnO: Al thin films by sol-gel technique, *Phys. B*, 2006, **381**, 209–213.
23 S. Das, *et al.*, Synthesis and characterization of boron antimonide films by pulsed laser deposition technique, *Appl. Surf. Sci.*, 2015, **353**, 439–448.
24 H. Badehian, *et al.*, Ab-initio study of the structural, electronic and optical properties of BSb (110) and (100) surfaces, *Surf. Sci.*, 2014, **628**, 1–7.
25 I. Mal, *et al.*, Origin of direct and indirect bandgap in B-X (X = Sb, Bi): A first principle study, *Mater. Today: Proc.*, 2021, **46**, 5870–5873.
26 R. Ahmed, *et al.*, Physical Properties of III-Antiminodes-a First Principles Study, *Commun. Theor. Phys.*, 2009, **52**, 527.
27 C. Ma, *et al.*, Broadband Nonlinear Photonics in Few-Layer Borophene, *Small*, 2021, **17**, 2006891.
28 I. Hasa, *et al.*, A rechargeable sodium-ion battery using a nanostructured Sb-C anode and P2-type layered Na0.6Ni0.22Fe0.11Mn0.66O2 cathode, *RSC Adv.*, 2015, **5**, 48928–48934.
29 P. Mishra, *et al.*, Study of air stability mechanism of 2D boron antimonide, *AIP Conf.*, 2019, **2142**, 110019.
30 X. Su, *et al.*, High Thermoelectric Performance in the Wide Band-Gap $AgGa_{1-x}Te_2$ Compounds: Directional Negative Thermal Expansion and Intrinsically Low Thermal Conductivity, *Adv. Funct. Mater.*, 2019, **29**, 1806534.
31 Z. Z. Zhou, *et al.*, A Comparative Study of the Thermoelectric Performance of Graphene-like BX (X = P, As, Sb) Monolayers, *J. Phys.: Condens. Matter*, 2019, **31**, 385701.
32 M. Al-Fartoos, *et al.*, Advancing Thermoelectric Materials: A Comprehensive Review Exploring the Significance of One-Dimensional Nano Structuring, *Nanomater*, 2023, 13, DOI: **10.3390/nano13132011**.
33 G. S. Nolas, J. Sharp and H. Julian Goldsmid, *Thermoelectrics*, Springer, Berlin, Heidelberg, 2001.
34 M. Zebarjadi, *et al.*, Perspectives on thermoelectrics: from fundamentals to device applications, *Energy Environ. Sci.*, 2012, **5**, 5147–5162.

